JOURNAL OF PROPULSION AND POWER
Vol. 12, No. 6, November–December 1996

Numerical Simulation of a Hydrogen Arcjet

V. Babu,* S. M. Aithal,† and V. V. Subramaniam‡
Ohio State University, Columbus, Ohio 43210

The two-dimensional, axisymmetric, nonequilibrium ionizing and reacting flow in a hydrogen arcjet thruster is simulated numerically using the linearized block implicit method. A single ionic species (H^+), single temperature (i.e., equal electron and heavy particle temperatures), and variable properties are used in this formulation to solve the governing equations of mass, species, momentum, and energy. The current distribution is obtained by solving the magnetic diffusion equation at each time step of the time-marching scheme. As an illustration, a hydrogen arcjet having an exit-to-throat area ratio of 25 (nominal 30-kW geometry) is studied. It is found that the species in order of their abundance at the centerline of the exit plane of the thruster consist of atomic hydrogen (H), ions (H^+), and electrons (e^-), and molecular hydrogen (H_2), respectively. As expected, near the colder walls of the anode at the exit plane, this abundance shifts in favor of molecular hydrogen, atomic hydrogen, H^+, and electrons, respectively.

Nomenclature

$\boldsymbol{B}$ = magnetic induction vector, 0, $-B_\theta$, 0
B_θ = azimuthal component of the magnetic induction
D_m = diffusion coefficient of diluent species m
E'_r, E'_x = radial and axial components of the electric field in the frame of reference moving with the local fluid velocity, $\boldsymbol{E}' = \boldsymbol{E} + \boldsymbol{u} \times \boldsymbol{B}$
e = internal energy per unit volume
j_r, j_x = radial and axial components of current density
k = thermal conductivity
k_B = Boltzmann's constant
m = atomic or molecular mass
N_d = number of diatomic species
N_m = number of diluent species
n_m = number density of diluent species m
n_T = total number density
p = pressure
R = gas constant of the propellant mixture at inlet
r, x = radial and axial coordinates
SRD = source term in species equation representing source due to spontaneous radiative emission
T = temperature
t = time
$\boldsymbol{u}$ = velocity vector
u, v, w = radial, azimuthal, and axial velocity components
VT = source term in species equation representing net production caused by vibrational–translational mode collisional energy exchange processes
VV = source term in species equation representing net production caused by vibrational–vibrational mode collisional energy exchange processes
$\Delta\varepsilon$ = change in energy of formation per unit volume, allows for change of reference state
ε_D = dissociation energy per particle
ε_i = ionization energy per particle
η = viscosity
μ = mobility
μ_0 = permeability of free space
ρ = mass density
σ = electrical conductivity
Φ = dissipation term in the energy equation

Subscripts
d = dissociation
el = electrodes
ep = exit plane
iep = input electrical power
i = ionization
th = thrust
tr = translational
v = viscous

Received Nov. 2, 1994; revision received Feb. 15, 1996; acccepted for publication Aug. 17, 1996.

*Postdoctoral Research Associate, Nonequilibrium Thermodynamics and Diamond Thin Films Laboratories, Department of Mechanical Engineering; currently Engineering Specialist, Scientific Research Laboratory 2113, Ford Motor Company, Dearborn, MI 48121.

†Graduate Research Associate, Nonequilibrium Thermodynamics and Diamond Thin Films Laboratories, Department of Mechanical Engineering.

‡Associate Professor, Nonequilibrium Thermodynamics and Diamond Thin Films Laboratories, Department of Mechanical Engineering. Senior Member AIAA.

I. Introduction

ARCJET thrusters impart directed kinetic energy to a propellant by ohmically heating it and subsequently expanding it in a supersonic nozzle. The arcjet consists of an inlet plenum where the propellant is sometimes injected with swirl, a converging portion, a straight section called the constrictor, and a diverging portion or supersonic nozzle as shown in Fig. 1. The arcjet is capable of operating on a variety of different propellants such as hydrazine, ammonia, and hydrogen. The flow enters the inlet plenum unionized, relatively cold, at subsonic speeds, and heats up near the cathode tip and at the entrance to the constrictor. The propellant is thus rapidly heated to near sonic speeds by the time it reaches the exit to the constrictor. Beyond the constrictor, i.e., in the nozzle, the flow is rapidly expanded to supersonic speeds. All the while, as the flow accelerates in the nozzle, it continues to be ohmically heated because of the arc attachment downstream of the constrictor on the anode (see Fig. 1). If not for the rapidly increasing cross-sectional area, the supersonic flow would be slowed down because of viscous effects and heat addition. The dynamics of this energy addition, and its subsequent conversion into directed kinetic energy is crucial in determining the arcjet's performance as a space propulsion system. It is this aspect of the device that we explore in this article.

It is perhaps easiest to think of the arcjet as an energy conversion device. Energy is primarily added upstream, in the converging and constrictor portions of the arcjet. After subsequent energy transfer and redistribution within the internal

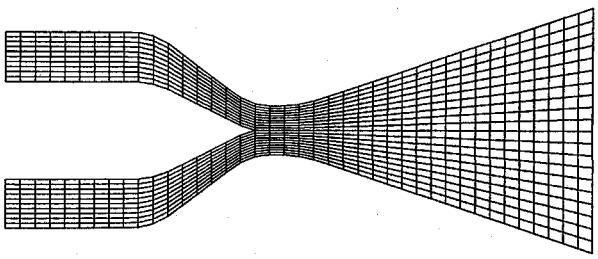

Fig. 1 Computational grid used in the numerical simulations. Note that computations are done on 60 × 50 and 120 × 50 grids. However, for plotting purposes, only every third axial and fifth radial grid locations are shown for the 120 × 50 grid.

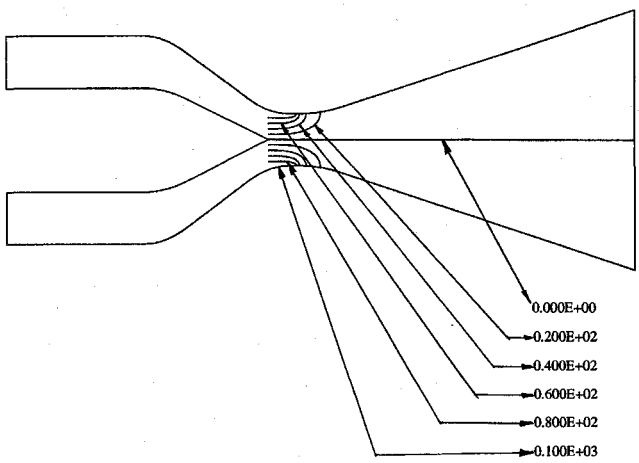

Fig. 2 Current contours for the 30-kW arcjet are shown here for a total current of 100 A.

and external modes of the propellant molecules, the input energy is converted into directed kinetic energy (i.e., useful thrust power) in the diverging supersonic nozzle. In classical gasdynamics terms, the arcjet flow includes the effects of heating (ohmic) and friction (viscous effects). Smooth and steady acceleration from subsonic to supersonic speeds therefore requires a delicate balance between heat addition, viscous effects, and area variation. As seen from Fig. 2, the arc attaches at the cathode tip so that the current is mainly axial in the converging and constrictor portions while the attachment downstream is radial on the anode walls. Consequently, there are both radial and axial components of the current in the supersonic, diverging portion. This renders the flow at least two dimensional so that simplified analytical approaches become limited in their usefulness, and there is no recourse but to solve the governing equations numerically. In this article, we discuss our formulation of the two-dimensional axisymmetric flowfield, but with three components of momentum.

II. Formulation

A. Governing Equations

The equations that govern the flow in arcjet thrusters are the compressible Navier–Stokes equations. In this case, these equations are more complicated than usual with variable properties, $j \times B$ body force, ohmic heating, species diffusion, and chemical reactions with ionization/recombination. We write the governing equations in their two-dimensional axisymmetric form with the nonzero azimuthal component of velocity. The continuity and momentum equations are given as[1]

$$\frac{\partial \rho}{\partial t} + \frac{1}{r}\frac{\partial}{\partial r}(r\rho u) + \frac{\partial}{\partial x}(\rho w) = 0 \tag{1}$$

$$\frac{\partial}{\partial t}(\rho u) + \frac{1}{r}\frac{\partial}{\partial r}(r\rho u^2) + \frac{\partial}{\partial x}(\rho u w) - \frac{\rho v^2}{r} = -\frac{\partial p}{\partial r} + \frac{\partial}{\partial r}\left(2\eta\frac{\partial u}{\partial r} - \frac{2}{3}\eta\nabla\cdot\boldsymbol{u}\right) - j_x B_\theta + \frac{\partial}{\partial x}\left[\eta\left(\frac{\partial u}{\partial x} + \frac{\partial w}{\partial r}\right)\right] + \frac{2\eta}{r}\left(\frac{\partial u}{\partial r} - \frac{u}{r}\right) \tag{2}$$

$$\frac{\partial}{\partial t}(\rho v) + \frac{1}{r}\frac{\partial}{\partial r}(r\rho u v) + \frac{\partial}{\partial x}(\rho v w) + \frac{\rho u v}{r} = \frac{\partial}{\partial r}\left[\eta\left(\frac{\partial v}{\partial r} - \frac{v}{r}\right)\right] + \frac{\partial}{\partial x}\left[\eta\left(\frac{\partial v}{\partial x}\right)\right] + \frac{2\eta}{r}\left(\frac{\partial v}{\partial r} - \frac{v}{r}\right) \tag{3}$$

$$\frac{\partial}{\partial t}(\rho w) + \frac{1}{r}\frac{\partial}{\partial r}(r\rho u w) + \frac{\partial}{\partial x}(\rho w^2) = -\frac{\partial p}{\partial x} + \frac{\partial}{\partial x} \times \left(2\eta\frac{\partial w}{\partial x} - \frac{2}{3}\eta\nabla\cdot\boldsymbol{u}\right) + j_r B_\theta + \frac{1}{r}\frac{\partial}{\partial r}\left[\eta r\left(\frac{\partial u}{\partial x} + \frac{\partial w}{\partial r}\right)\right] \tag{4}$$

In the previous equations, the magnetic field is assumed to have only an azimuthal component ($-B_\theta$). The energy equation is written for transport of total energy, i.e., internal energy and kinetic energy, under the assumption that a single temperature (i.e., equal electron and heavy particle temperature) exists:

$$\frac{\partial e_T}{\partial t} + \frac{1}{r}\frac{\partial}{\partial r}[(e_T + p)ur] + \frac{\partial}{\partial x}[(e_T + p)w] = \frac{1}{r}\frac{\partial}{\partial r}\left(kr\frac{\partial T}{\partial r}\right) + \frac{\partial}{\partial x}\left(k\frac{\partial T}{\partial x}\right) + \eta\Phi + j_r w B_\theta - j_x u B_\theta + \frac{j_r^2 + j_x^2}{\sigma} \tag{5}$$

where

$$e_T = e + \rho(u^2 + v^2 + w^2)/2$$

In the previous equation, e is given by[2]

$$e = \frac{3}{2}n_T k_B T + \sum_{i=1}^{N_d} n_i k_B T + \sum_{i=1}^{N_d}\sum_{v=0}^{V_{max}} n_{i,v}E_{i,v} + \Delta\varepsilon$$

and equilibrium is assumed between the translational and rotational modes of molecular motion. The detailed form for Φ can be found in Ref. 3. It is important to note that where molecular species are present in appreciable quantities in a discharge, the electrons are not governed by a single temperature.[4] Consequently, Eq. (5) would describe the heavy particles, while the electron energy equation would have to be replaced by a Boltzmann equation for the electron energy distribution function (EEDF). While this is expected to be the case for propellants such as ammonia and hydrazine, hydrogen may be described adequately by a temperature (representing an average translational energy, assuming that the energy distribution function is log–linear vs energy). In the present formulation, we consider a mixture of H_2, H, H^+ (protons), and electrons (e^-), and further assume that electron and heavy particle temperatures are equal. The species equations can then be written as

$$\frac{\partial n_m}{\partial t} + \frac{1}{r}\frac{\partial}{\partial r}(u n_m r) + \frac{\partial}{\partial x}(n_m w) + \frac{1}{r}\frac{\partial}{\partial r}\left[-r n_m \mu_m E_r' - \frac{r D_m}{kT}\frac{\partial}{\partial r}(n_m kT)\right] + \frac{\partial}{\partial x}\left[-n_m \mu_m E_x' - \frac{D_m}{kT}\frac{\partial}{\partial x}(n_m kT)\right] = \dot{n}_m \tag{6}$$

where the subscript m takes on values from 1 to N_m. In the previous equations, $p = n_T k_B T$, where $n_T = \sum_{m=1}^{N_m} n_m + \sum_{i=1}^{N_d} \sum_{v=0}^{V_{max}} n_{i,v} \cdot \dot{n}_m$ represents the net production of species m because of chemical reactions and include ionization and recombination processes. A continuity equation similar to Eq. (6) can be written for diatomic species:

$$\frac{\partial n_{i,v}}{\partial t} + \frac{1}{r}\frac{\partial}{\partial r}(u n_{i,v} r) + \frac{\partial}{\partial x}(n_{i,v} w) + \frac{1}{r}\frac{\partial}{\partial r} \times \left[-r n_{i,v}\mu_{i,v}E_r' - \frac{r D_{i,v}}{kT}\frac{\partial}{\partial r}(n_{i,v}kT)\right] + \frac{\partial}{\partial x}\left[-n_{i,v}\mu_{i,v}E_x' - \frac{D_{i,v}}{kT}\frac{\partial}{\partial x}(n_{i,v}kT)\right] = \dot{n}_{i,v} + VT_{i,v} + VV_{i,v} + SRD_{i,v} \quad (7)$$

In the present calculations, discrete vibrational states are not considered so that the *VT*, *VV*, and *SRD* terms are zero. Thus, Eq. (7) for the molecular species reduces in form to Eq. (6). The mass density is related to the number densities through the following algebraic relation:

$$\rho = \sum_{k=1}^{N_m} m_k n_k + \sum_{i=1}^{N_d} m_i \sum_{v=0}^{V_{max}} n_{i,v} \quad (8)$$

We now turn to the formulation of the electromagnetics that is governed by Maxwell's equations. A single equation for magnetic transport under steady-state conditions can be obtained from Maxwell's equations by using a well-known vector identity.[3] Inclusion of the time derivative via the $\mu_0\sigma(\partial \boldsymbol{B}/\partial t)$ term would force us to resolve extremely small time scales involving the inverse of the speed of light. This would be computationally very intensive, and unnecessary when seeking a steady-state solution. Using Ampere's law ($\nabla \times \boldsymbol{B} = -\mu_0\sigma(\boldsymbol{E} + \boldsymbol{v} \times \boldsymbol{B})$, expanding the cross products, and using the well-known vector identity: $\nabla \times (\nabla \times \boldsymbol{B}) = -\nabla^2 \boldsymbol{B} + \nabla(\nabla \cdot \boldsymbol{B}) = -\nabla^2 \boldsymbol{B}$, Maxwell's equations can be written in strong conservation form for a single component B_θ as follows:

$$\frac{1}{r}\frac{\partial}{\partial r}\left(\frac{r}{\sigma}\frac{\partial B_\theta}{\partial r}\right) + \frac{\partial}{\partial x}\left(\frac{1}{\sigma}\frac{\partial B_\theta}{\partial x}\right) + \frac{B_\theta}{r}\frac{\partial}{\partial r}\left(\frac{1}{\sigma}\right) - \mu_0\frac{\partial}{\partial x}(wB_\theta) - \mu_0\frac{\partial}{\partial r}(uB_\theta) = 0 \quad (9)$$

This formulation in terms of B_θ is necessary because we are including $\boldsymbol{j} \times \boldsymbol{B}$ body forces, which we believe are important in some regions of the flow as do the authors of Ref. 5. For arcjet flows, the last two terms in Eq. (9) are small and can be neglected. Equation (9) is solved numerically in conservative form (exactly as written earlier) without the inclusion of these last two terms. This is in contrast to the formulation of Ref. 6, which essentially follows that of Ref. 7, in which $\boldsymbol{j} \times \boldsymbol{B}$ forces are neglected. In such a case, the electromagnetics problem is formulated in terms of the scalar potential governed by a Poisson equation, and voltages are then prescribed at the anode and cathode as boundary conditions. This is a crucial difference between the present work and other existing work.[5-9]

Equations (1–9) represent nine equations in the nine unknowns ρ, u, v, w, T, n_e, n_H, n_{H_2}, and B_θ in the present case. The formulation of the problem is not complete until boundary and initial conditions are specified. These are discussed next.

B. Boundary Conditions

Boundary conditions need to be specified for Eqs. (1–7) and (9), to complete the problem formulation. No-slip boundary conditions are prescribed for the velocity components on all solid surfaces. A symmetry condition is imposed for the axial component of velocity w, (i.e., $\partial w/\partial r = 0$ @ $r = 0$), whereas the other components of velocity (u and v) are set to zero along the centerline. (It can be shown formally from the conservation equations that applying symmetry conditions on u and v is equivalent to setting u and v to 0 at the centerline.) At the inlet boundary, u is set to zero, v is usually set to a prescribed distribution to simulate swirl (zero for the case studied in this article), and w is evaluated by using implicit extrapolation. At the exit plane, all of the velocity components are evaluated using implicit extrapolation. Implicit extrapolation refers to setting the second derivative of a particular dependent variable to zero in a given coordinate direction.

The temperature on the anode is set to 1000 K in the inlet plenum region until the beginning of the converging portion. Thereafter, the anode temperature is increased linearly up to 2000 K at the constrictor and maintained at this value until the exit region. The temperature on the cathode is evaluated by implicit extrapolation in the radial direction, which is equivalent to setting $\partial^2 T/\partial r^2 = 0$ at the cathode surface. This is different from other works[5-9] where a temperature distribution is prescribed on the cathode surface with a maximum at the cathode tip. Prescription of cathode temperature usually gives rise to difficulties at the tip such as the density becoming negative, since the temperature jumps from a few 1000 degrees Kelvin at the tip to tens of thousands of degrees Kelvin just a short distance downstream. The implicit extrapolation boundary condition on the cathode surface used in the present work alleviates this difficulty by reducing the gradient of the temperature in the vicinity of the tip. In reality, since the cathode tip is hot enough to be molten, such a boundary condition there is not entirely unrealistic. Symmetry is imposed on the temperature along the centerline (i.e., $\partial T/\partial r = 0$ @ $r = 0$). At the inlet, prescribing the stagnation temperature allows the static temperature to be evaluated once the velocity components are known. At the exit plane, the temperature is evaluated by implicit extrapolation.

Number densities on all of the solid surfaces are evaluated by implicit extrapolation in the radial direction. This is justifiable since processes occurring on the scale of sheath thicknesses (Debye length) are not considered here. In addition, this has proved to be most stable numerically. The number densities along the centerline are obtained by using symmetry (i.e., $\partial n_m/\partial r = 0$ @ $r = 0$). At the exit plane, the number densities are calculated by using implicit extrapolation. At the inlet, the number densities are obtained by implicit extrapolation. We have previously found that this assumption does not influence the solution downstream.[10,11]

Mass density on the solid surfaces is evaluated by implicit extrapolation. Density along the centerline is obtained from the symmetry condition (i.e., $\partial \rho/\partial r = 0$ @ $r = 0$). The stagnation pressure is specified at the inlet, from which the mass density can be determined once the temperature is known. At the exit, the mass density is computed by implicit extrapolation if the flow is supersonic at the given point, or from a specified static pressure if the flow is subsonic at that point.

We now turn to the boundary conditions for the magnetic transport equation. Solution of the magnetic diffusion equation is confined to downstream of a specific axial station, which in the present case is taken to be the cathode tip. Along the radial plane adjacent to the cathode tip, the radial current density is set to 0 or $\partial B_\theta/\partial x = 0$. B_θ is set to zero along the centerline (this is tantamount to imposing symmetry on the magnetic induction at the centerline) and along the exit plane to prevent the current from blowing out of the thruster. The anode is assumed to be a perfect conductor downstream from the middle of the constrictor region, and thus the current streamlines enter the anode surface normal to it. This is imposed by setting $(\nabla \times \boldsymbol{B}) \cdot \boldsymbol{s} = 0$, where $\boldsymbol{s}$ is the unit tangent vector along the anode surface. B_θ is prescribed a value based on the total en-

closed current over the first half of the constrictor wall. These conditions in effect prevent current attachment on the upstream half of the constrictor wall, and are necessary to obtain downstream arc attachment since the phenomena governing breakdown (initiation of the discharge at a given location) and extinction are not modeled.

C. Initial Conditions

It is extremely important to specify appropriate initial conditions to obtain stable solutions. The radial velocity is set to zero everywhere at the beginning of the calculations, while the axial velocity is given a linear variation from a small value at the inlet to a higher subsonic value at the exit. The initial temperature distribution is such that the temperature increases linearly from a value equal to the prescribed stagnation temperature of 1000 K at the inlet to a maximum of 10,000 K in the constrictor region, thereafter staying constant in the constrictor, and then decreasing linearly to an exit value of 2000 K. The initial pressure distribution is prescribed such that it is kept constant at the stagnation pressure until the beginning of the converging portion, and then decreased linearly to a specified value at the exit. The mass density at each axial section is then calculated from these initial pressure and temperature distributions. The number densities of all the other species (except one) are initially given either constant values or their distributions separately specified. The number density of the remaining specie is then calculated from the algebraic relationship between the prescribed mass density and the other prescribed number densities. The specific magnitude of the values used for these initial guesses do not impact the final converged results; however, the initial profiles and magnitudes do need to be reasonable. No initial distributions are required for the magnetic induction as it is governed by an elliptic equation [Eq. (9)]. It is important to note that since the magnetic transport is modeled by an elliptic equation, the burden of a good initial guess rests upon reasonable initial profiles for number densities and temperature.

D. Properties

We evaluate the coefficient of viscosity, thermal conductivity, and the species diffusivities using mean-free-path theory.[12] It is important to note that properties evaluated using mean-free-path theory can lead to discrepancies of a factor of 2 or 3.[12] The electrical resistivity is calculated as the sum of an electron-neutral resistivity and a Spitzer–Harm resistivity.[12] In the present work, we use a conductivity floor of 40 mho/m. In colder regions of the flow, the discretized form of Eq. (9) can be confronted with the loss of diagonal dominance. Consequently, there exists a minimum value of the conductivity below which stable numerical solutions cannot be obtained. In this work, the specific value of the conductivity floor is fixed on the basis of the required input electrical power, and is therefore not an adjustable parameter.

III. Numerical Method

The Linearized Block Implicit (LBI) method, developed by Briley and McDonald,[13] is used to solve Eqs. (1–7) numerically. The details of how we have adapted this method to solve the governing equations are discussed in detail elsewhere,[10,11] and therefore, only a brief summary is given here. The governing equations are written in strong conservation form, discretized in time using the Crank–Nicolson scheme, and then linearized about the previous time step using a Taylor series first-order accurate in time. A second-order dissipation term similar to that reported in Ref. 13 is added for stability. These linearized equations (and boundary conditions) are then discretized in space to second-order accuracy, after transforming from a uniform grid in the physical domain to a uniform grid in the computational domain.[14] (The grid in the physical domain could also be non-uniform, although here we use a uniform grid.) The two-dimensional operator is then split consistently into two one-dimensional operators using the Douglas–Gunn alternating direction implicit scheme. This results in a series of block tridiagonal systems (with block sizes equal to the number of unknowns at each point), which can be solved efficiently using standard LU (lower triangular upper triangular) decomposition methods.[15] The magnetic transport equation is solved separately at each time step of the time-marching process, using the odd–even Jacobi iterative scheme.

IV. Results for the Hydrogen Arcjet

Although the foregoing sections address a general approach for simulating nonequilibrium flows in arcjets, we present results here for the nominal 30-kW arcjet geometry[16] with H_2 as the propellant. This geometry is shown in Fig. 1. The results presented here do not include internal modes of energy storage of the propellant molecules such as vibration or electronic excitation. We further assume that the species present are H_2 molecules, H atoms, H^+ ions, and electrons. (Gaseous hydrogen consists of a mixture of two types known as ortho and para. In this work, we ignore this distinction.) Hence, N_m is equal to 2 and N_d equals 1. Since H_2 is the only diatomic species present and its vibrational states are neglected, a separate species conservation equation [such as Eq. (7)] need not be solved. Rather, the number density of H_2 can be found from the algebraic relationship, Eq. (8). The quantity $\dot{n}_m$ has to be evaluated from the specific chemical reactions that are being modeled. In the present case, we consider the following four processes in both forward and reverse directions:

$$H_2 + H_2 \Leftrightarrow H + H + H_2 \tag{10}$$

$$e^- + H \Leftrightarrow H^+ + e^- + e^- \tag{11}$$

$$H_2 + e^- \Leftrightarrow H + H + e^- \tag{12}$$

$$H + H_2 \Leftrightarrow H + H + H \tag{13}$$

The forward rates for reactions (10) and (13) are given in Ref. 17 whereas those for reactions (11) and (12) are given by Janev et al.[18] The reverse rates can be computed from the forward rates and the equilibrium constant based on partition functions.[2] In linearizing the $\dot{n}_m$ term, the forward and reverse rates are treated explicitly while the number densities that multiply them are treated implicitly. This improves the overall stability of the method while allowing different rate models to be included easily. A 60 × 50 grid was initially used for these calculations. Grid convergence studies were performed using a finer 120 × 50 grid, which is shown in Fig. 1. The maximum discrepancy between the coarser and finer grid results was less than 0.1%. We therefore report on the finer grid steady-state results here.

Contours of enclosed current defined as rB_θ are plotted in Fig. 2. The input current is 100 A and is represented by the constant value of B_θ imposed on the upstream half constrictor portion of the anode. The contours can be seen to concentrate within the downstream half of the constrictor, with some on the diverging section of the anode. The current densities and, hence, the ohmic heating, are quite large in the constrictor. The effects of this heating can be seen in Fig. 3, where the temperature along the cathode surface and along the channel centerline is shown. The maximum temperature of 39,480 K occurs at the cathode tip. Figure 4 shows the variation of temperature in the radial direction at the exit plane. Since the maximum exit temperature is approximately 4500 K, clearly much of the input energy is still bound in random translational motion as opposed to directed kinetic energy. The temperature profile at the exit plane also exhibits a bulge near the anode. This is caused by heating of the flow resulting from recombination of atomic hydrogen into molecular hydrogen near the cooler walls. This local temperature maximum is also en-

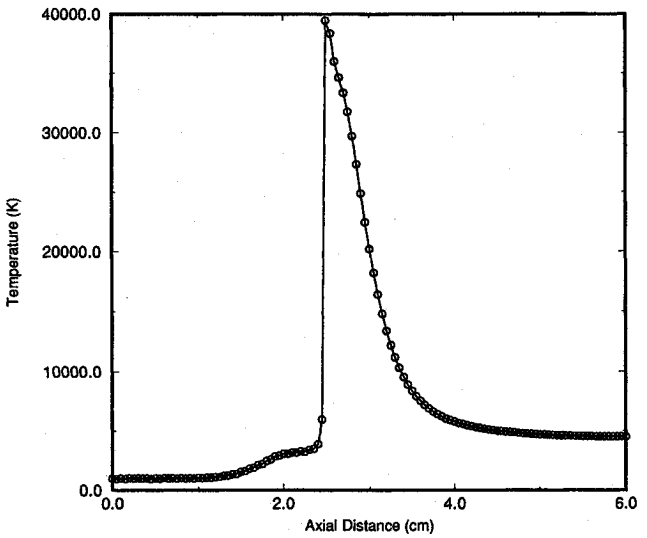

Fig. 3 Temperature at the centerline is shown here vs axial location.

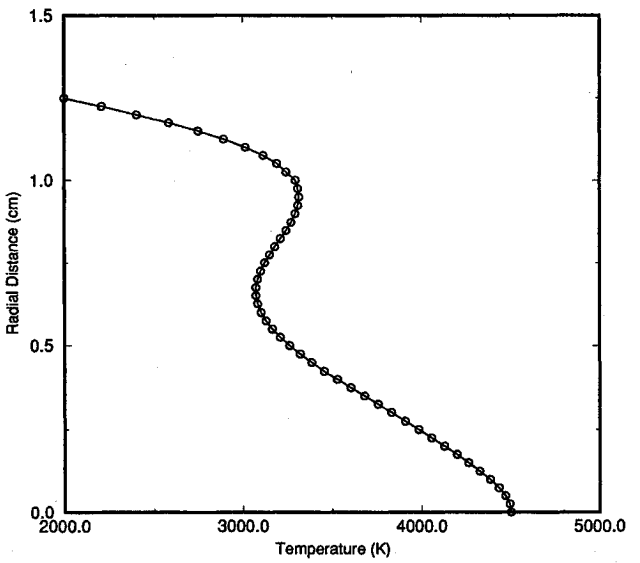

Fig. 4 Variation of temperature in the radial direction at the exit plane.

hanced by the opposing effects of viscous dissipation and wall cooling. Figure 5 shows contours of the temperature.

The variation of the streamwise component of the velocity w along the centerline is shown in Fig. 6. As expected from classical gasdynamics, the deceleration of the velocity can be seen in the latter portion of the diverging section of the arcjet. This is because of the well-known slowing down of a supersonic flow caused by heat addition and viscous effects. Figure 7 shows the variation of w at the exit plane. As is evident, the velocity profile exhibits a shape that implies a highly viscous flowfield. Mach contours are shown in Fig. 8, where the Mach number is defined as w divided by $\sqrt{5RT/3}$. The maximum Mach number of 3.23 is reached within the arcjet in the diverging section and decreases toward the exit plane.

Radial profiles of electron number density at several axial locations are shown in Fig. 9, with the maximum occurring at the centerline. The corresponding radial variation at the exit plane is shown in Fig. 10, again exhibiting a maximum value at the centerline. It is important to note that the highest value of the ionization fraction found in this work is about 0.125, while the highest value reported in Ref. 6 is 1.0. This discrepancy cannot be reconciled because no information on neutral

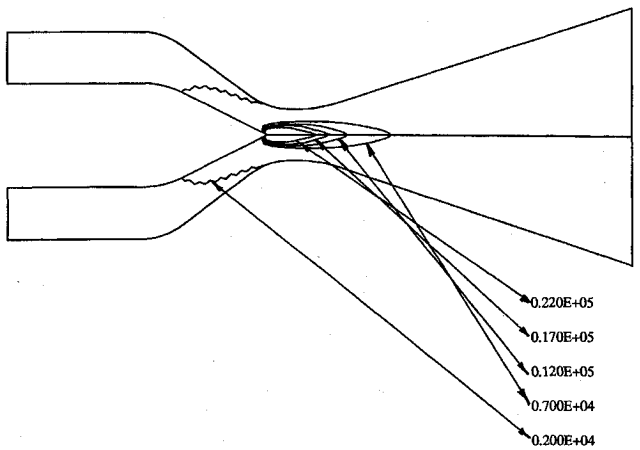

Fig. 5 Contours of temperature.

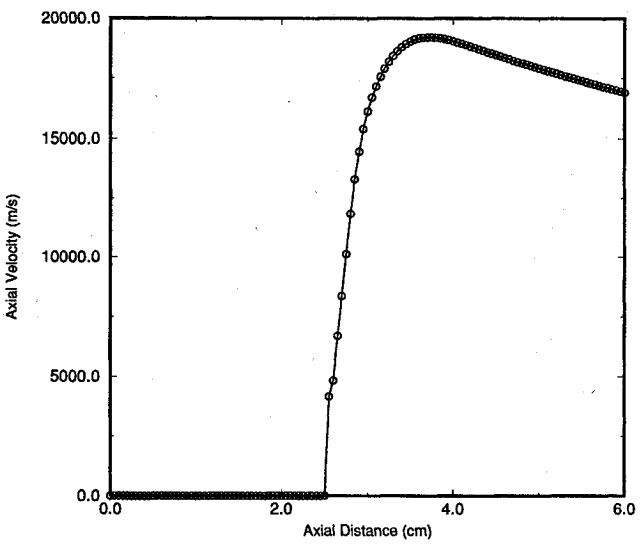

Fig. 6 Variation of w in the axial direction.

species concentrations is provided in Ref. 6. However, the maximum value of ~0.125 for the ionization fraction reported in this work is self-consistent, based on the fact that the local residence time of the flow is found to be much shorter than the characteristic time required for ionization. The H atom number densities in the constrictor region are shown in Fig. 11, and display a local maximum away from the centerline. This is because of the opposing effects of dissociation caused by ohmic heating near the centerline and recombination caused by the presence of a relatively colder wall. A similar profile is also seen at the exit plane, as shown in Fig. 12. Because of the high temperatures in the constrictor region, H_2 dissociation by various mechanisms is also active. The ionization reaction being the fastest, consumes H atoms rapidly, thereby producing increasing numbers of electrons. As a result of the lower temperatures in the regions toward the wall, recombination is more active than ionization and the electron number density falls. As can be expected, the H_2 number densities shown in Fig. 13 increase all the way from a minimum at the centerline to a maximum at the wall. A similar shape is also seen at the exit plane (see Fig. 14). Contours of dissociation fraction are shown in Fig. 15. Interestingly, a substantial amount of atomic hydrogen can be seen exiting the thruster. Since molecular hydrogen is the propellant introduced into the arcjet in the first place, appreciable amounts of atomic H at the exit plane signify frozen low losses mainly arising from redistribution of input electrical energy into dissociation. H_2 and H are the predominant species at the exit plane with particle flow rates of

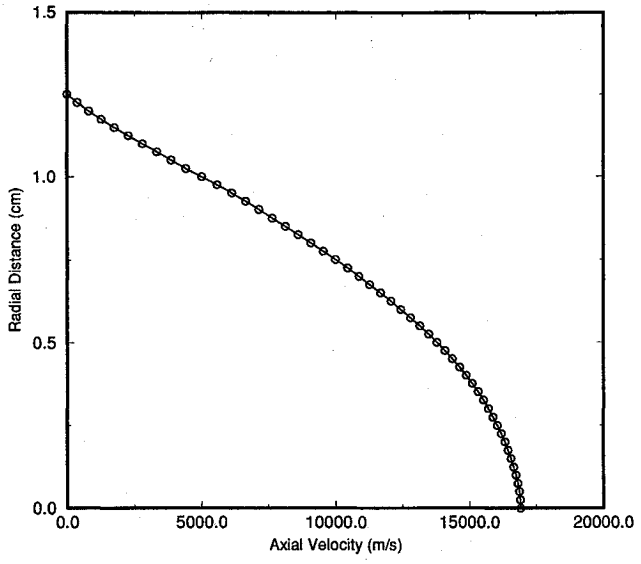

Fig. 7 Variation of w in the radial direction, at the exit plane.

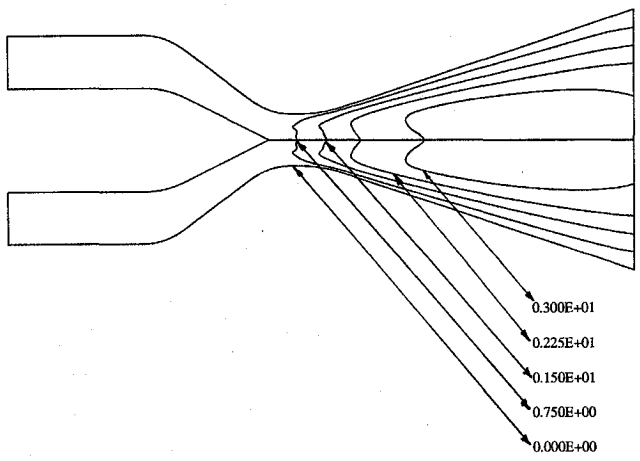

Fig. 8 Contours of Mach number.

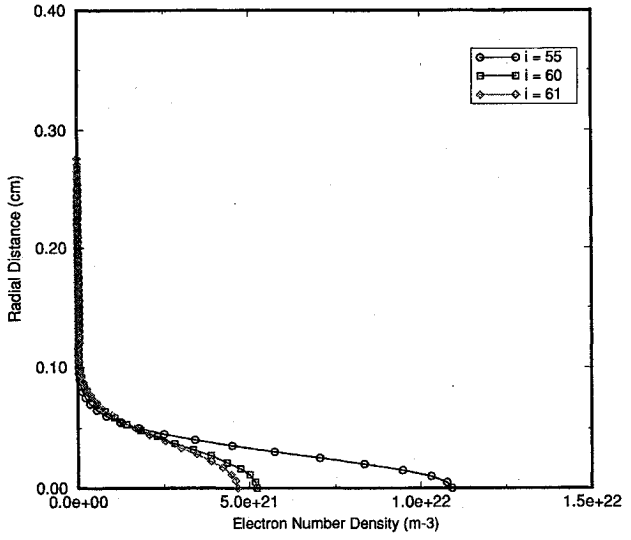

Fig. 9 Radial variations of the electron number density at various axial locations in the middle of the constrictor (i = 55), at the exit of the constrictor (i = 60), and just beyond the constrictor (i = 61). Note that the maximum values occur at the centerline, as expected.

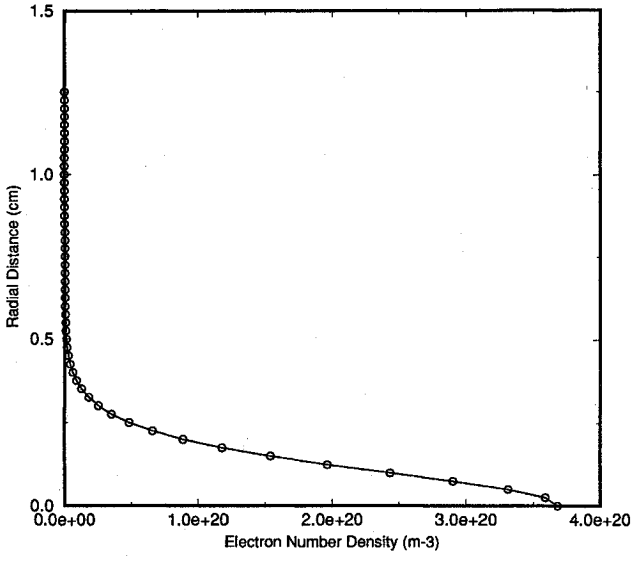

Fig. 10 Radial variation of the electron number density, at the exit plane.

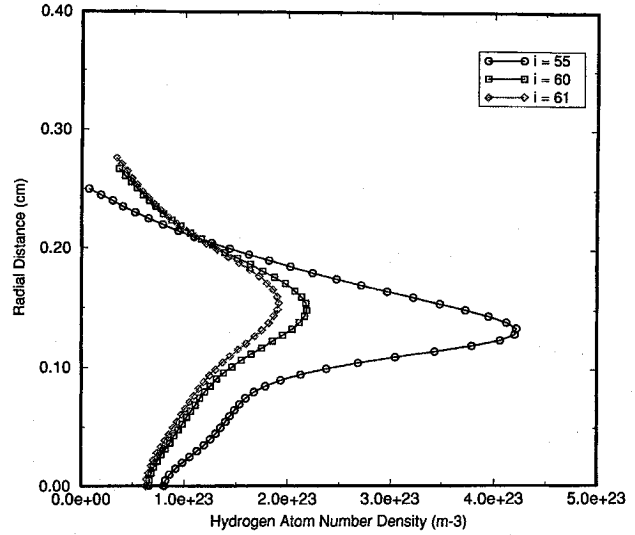

Fig. 11 Radial variations of H atom number density at the same axial locations as in Fig. 9.

2.22×10^{22} and 1.92×10^{22} s^{-1}, respectively. The impact of this result on frozen flow losses is discussed in the following section.

Finally, the terminal voltage can be determined from the computed electric field $\boldsymbol{E}$:

$$V(x) = \int_{P(x)} \boldsymbol{E} \cdot d\boldsymbol{l}$$

where $\boldsymbol{E} = (\boldsymbol{j}/\sigma) - \boldsymbol{u} \times \boldsymbol{B}$, and the integration is performed along a path $P(x)$ beginning at the cathode tip, extending axially downstream along the channel centerline, and then proceeding radially outward to the anode surface. In this manner, a terminal voltage distribution $V(x)$ is obtained. This distribution is shown in Fig. 16. The mean value of the voltage over this interval can be evaluated by numerically integrating the distribution shown in Fig. 16 over the complete interval, to yield 244 V. However, most of the voltage distribution shown in Fig. 16 shows a constant value of 126 V. It would be erroneous to compute the input electrical power on the basis of these average values of the terminal voltage and the total current because the electrical conductivity is not a constant.

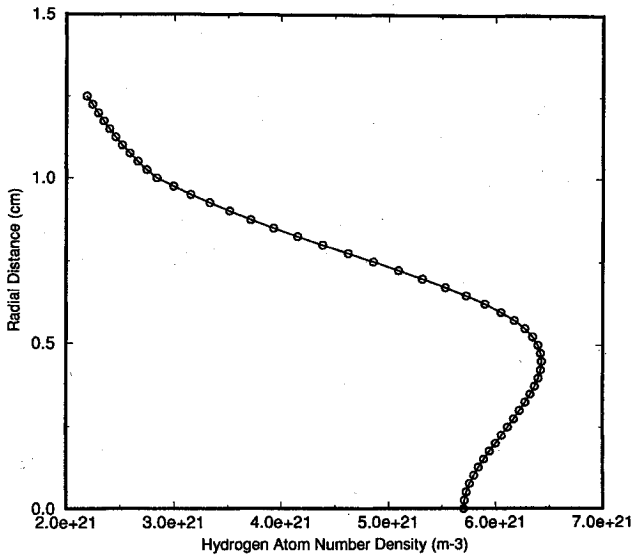

Fig. 12 Radial variation of the H atom number density, at the exit plane.

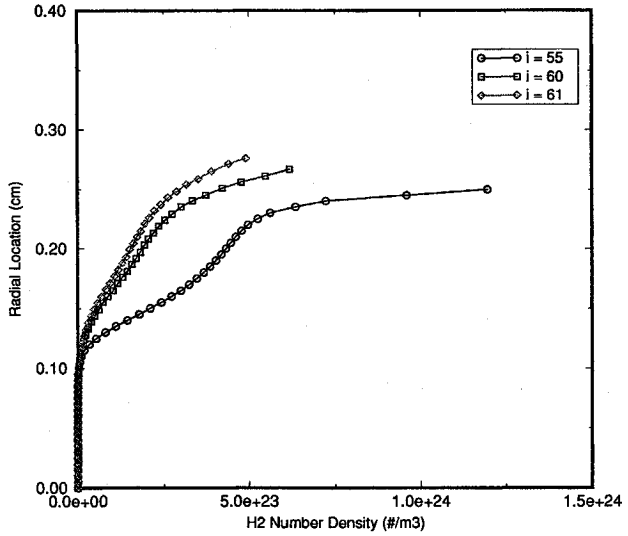

Fig. 13 Radial variations of the number density of H_2 at the same axial locations as in Fig. 9.

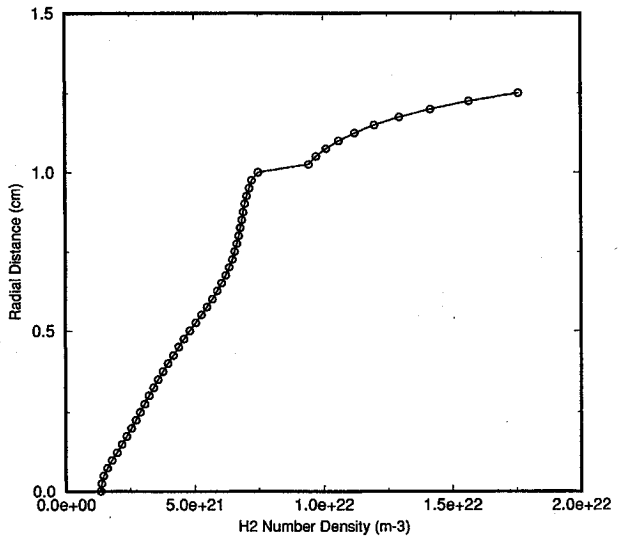

Fig. 14 Radial variation of the molecular hydrogen number density at the exit plane.

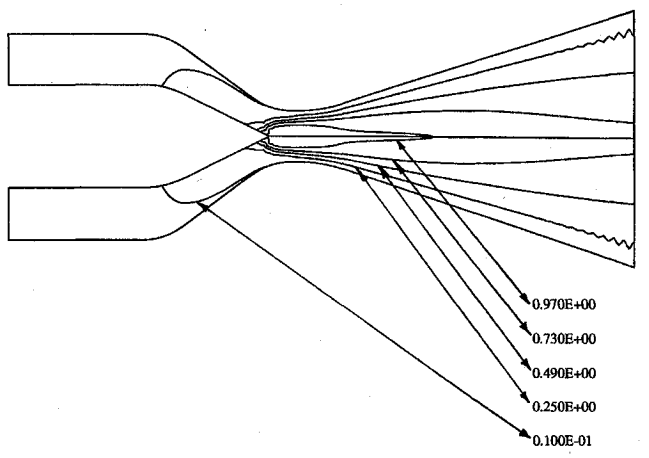

Fig. 15 Contours of dissociation fraction β [defined as $n_H/(n_H + n_{H_2})$].

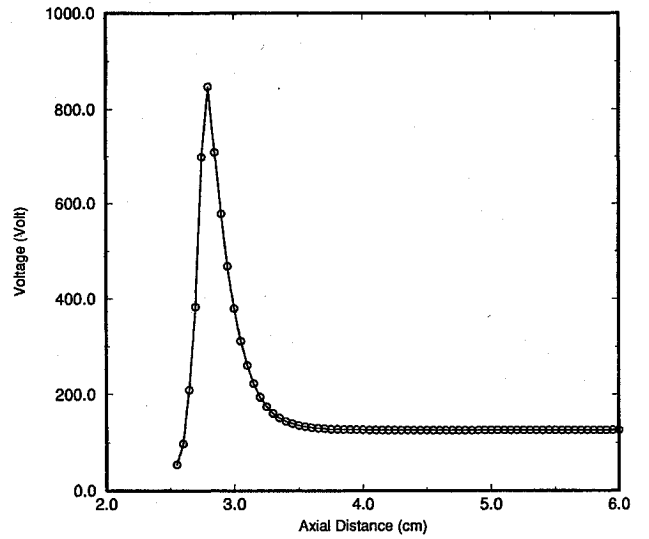

Fig. 16 Distribution of computed voltage vs axial distance. The terminal voltage is determined by $\int E \cdot dl$ along a path beginning from the cathode tip, extending along the centerline and then vertically (i.e., radially) outward ending at the anode surface. This method is essentially the same as reported in Ref. 11.

Rather, the input electrical power must be computed by integrating $E \cdot j$ over the volume enclosed by the thruster. This value for the present case is 30.5 kW.

V. Discussion of Results

The results presented in the previous section were for a hydrogen arcjet (nominal 30-kW geometry) operating with a mass flow rate of 100 mg/s. This mass flow rate was computed after prescription of a particular upstream total pressure. For this case, the calculated specific impulse was 1037 s. Experimental test results as well as the results of other numerical simulations for conditions similar to those studied in Sec. IV (total current of 100 A and mass flow rate of 100 mg/s) do exist.[6,16]

A comparison between our present results and those of Refs. 6 and 16 are displayed in Table 1. Before conclusions can be drawn from this comparison, it is important to highlight a key point. The total current in this work is maintained at 100 A, consistent with Refs. 6 and 16. However, the power levels reported in Refs. 6 and 16 are based on a product of terminal voltage and total current. In contrast, we compute the total electrical power into the thruster on the basis of a volume integral of $E \cdot j$ consistent with Poynting's theorem.[3] These aforementioned differences, while having a minimal effect on

Table 1 Comparison of predicted performance with existing work

Operating characteristics	This work (numerical)	Ref. 9 (numerical)	Ref. 16 (experimental)
Total current	100 A	100 A	100 A
Terminal voltage	See Fig. 16	115 V	112 V
Mass flow rate	105 mg/s	100 mg/s	100 mg/s
Power	30.5 kW[a]	11.5 kW	11.2 kW
Specific impulse	1037 s	1030 s	960
Thrust efficiency	42.7%[b]	44.2%	39.5%

[a]This value of the power is obtained from Eq. (15). If the value of 126 V as given by the constant portion of Fig. 16 is multiplied by 100 A, then an input electrical power of 12.6 kW is obtained.
[b]This value is obtained by dividing the thrust power at the exit plane by the integrated value of the electrical power input as given by Eq. (15).

comparisons of specific impulse, can have a significant effect on the thrust efficiency.

The differences between our predictions and those of previous work[5,16] are a result of formulation of the electromagnetics, as well as the chemical kinetics. In our formulation, it is not possible to fix the terminal voltage a priori. Rather, the voltage is determined upon solution of the magnetic diffusion equation followed by use of Ohm's law [$j = \sigma(\boldsymbol{E} + \boldsymbol{u} \times \boldsymbol{B})$].

It is useful to quantify the different channels by which input electrical energy is redistributed within the propellant. Indeed, such an approach is helpful in identifying the dominant energy loss pathways. It is also a measure of how well our numerical simulation satisfies overall conservation of energy. This is a measure that has not been applied in previous work.[5-9] Consider therefore, an overall energy balance on a control volume encompassing the propellant flow inside the arcjet, bounded by the electrodes, and the exit plane:

$$Q_v - Q_{el} + \iiint (\boldsymbol{E}\cdot j)\, dV = \int_0^{r_o} \left(3n_e + \frac{3}{2} n_H + \frac{5}{2} n_{H_2}\right)_{ep} k_B T w 2\pi r\, dr + \int_0^{r_o} (\rho w^3)_{ep}\, 2\pi r\, dr + \int_0^{r_o} (n_H w \varepsilon_D)_{ep}\, 2\pi r\, dr + \int_0^{r_o} (n_e w \varepsilon_i)_{ep}\, 2\pi r\, dr = Q_{tr} + P_{th} + Q_d + Q_i \qquad (14)$$

where Q_{el} is that portion of the input electrical power that is consumed in heating of the electrodes and other components; Q_v represents that portion of the input power that results in heating caused by viscous effects; Q_{tr} is the portion of the input power bound into random thermal energy per unit time (i.e., translational motion, not including any internal degrees of freedom); P_{th} is the thrust power; and Q_d is the energy lost per unit time in dissociation, with ε_D being the dissociation energy per molecule and ε_i the ionization energy per particle.

The operating power level is evaluated a posteriori in our formulation. This appears to be in contrast to other existing work,[5-9] where the power level is set in the form of a total current and an average terminal voltage. It can be misleading to compute power input into the discharge of the arcjet as a product of the total current and terminal voltage. A more appropriate means of determining the total input electrical power is via Poynting's theorem:

$$P_{iep} = \int_0^L \int_{r_i(x)}^{r_o(x)} (E\cdot j) 2\pi r\, dr\, dx \qquad (15)$$

where $r_i(x)$ and $r_o(x)$ are the inner radius and outer radius of the channel varying along the axial coordinate x, respectively, and L is the length of the thruster. According to Eq. (15), the electrical power input in the case of the hydrogen arcjet simulation results presented in Sec. IV is 30.5 kW.

Each of the quantities given in Eq. (14) can be evaluated numerically. The translational power loss based on the results obtained in Sec. IV is found to be 3.831 kW, whereas the thrust power is 13.034 kW. In contrast, 13.685 kW is expended to produce the high flux of atomic hydrogen exiting the thruster. Consequently, the thrust efficiency (i.e., thrust power divided by total input electrical power), without accounting for heat loss and viscous dissipation, is approximately 42.7%.

From the foregoing discussion, a substantial amount of energy is clearly invested in dissociation of molecular hydrogen for the case of hydrogen propellant. Unfortunately, this is not the only form of frozen flow loss. In the present work, we have neglected energy transfer into electronic states of both molecular and atomic hydrogen. Therefore, the actual efficiency is likely to be lower than the predicted value of 42.7% reported here.

VI. Summary and Conclusions

A numerical simulation of the flow in a hydrogen arcjet with an exit-to-throat area ratio of 25 has been presented. The present work utilizes the fully implicit LBI method first developed by Briley and McDonald[13] and has demonstrated a good potential for handling the stiffness problems usually arising in chemically reacting and ionizing flows. Results from this simulation, especially relating to arcjet performance, have been compared and contrasted with those of previous experiments and simulations[6,16] for similar conditions. However, there are significant differences in the maximum ionization level (as well as species concentrations) found in the present work and those of Ref. 6. The exact nature of this discrepancy cannot be determined since details related to species concentrations are not provided in Ref. 6. The present approach also shows that care must be exercised when evaluating the total power input into the propellant flow. The total electrical power into the arcjet discharge must be evaluated by $\iiint (\boldsymbol{E}\cdot\boldsymbol{j})\, dVol$, and not simply by multiplying the terminal voltage and the total current. This is especially crucial when evaluating thrust efficiency. The present work shows that a substantial fraction of the exit plane flow consists of atomic hydrogen, and constitutes the biggest frozen flow loss for the hydrogen arcjet.

It is clear from Eq. (14) that for any arcjet to function as a desirable propulsion system, the thrust power must be maximized. All other terms on the right-hand side (RHS) of Eq. (14) represent losses, and therefore contribute to lowering the efficiency and specific impulse. If other modes of energy storage such as vibrational energy (especially important for propellants such as hydrazine and ammonia), rotational energy, or electronic excitation are included, then these would constitute additional losses and would appear on the right-hand side of Eq. (14). The first term on the RHS of Eq. (14) represents that portion of input power that is bound in random thermal motion (as measured by the static temperature). As can be seen from

our simulations as well as from experiment, the static temperature at the exit of the arcjet can be significant (~4500 K at the centerline). This represents energy that has not been converted into directed kinetic energy in the nozzle, and is a recoverable loss. One way to recover this energy may be to continue the expansion (e.g., by adding an electrically insulated extension to the anode or nozzle). Unfortunately, this would add length to the device, thereby increasing viscous losses. Yet another way would be to cool the anode wall, especially on the supersonic side. As difficult as the task may be, experimental measurements related to the location of arc attachment on the anode inside the arcjet would provide valuable guidance to improve the state of the art in modeling of arcjet flows.

Acknowledgments

This work was supported by the U.S. Air Force Office of Scientific Research Grant 91-0318 and F49620-94-1-0015. We also gratefully acknowledge Grant PAS745-1 from the Ohio Supercomputer Center and the use of their Cray Y-MP. The authors acknowledge helpful discussions with W. R. Briley.

References

[1]Todreas, N. E., and Kazimi, M. S., *Nuclear Systems I—Thermal Hydraulic Fundamentals*, Taylor and Francis, Washington, DC, 1990, p. 115.

[2]Vincenti, W. G., and Kruger, C. H., *Introduction to Physical Gas Dynamics*, Krieger, Malabar, FL, 1986, pp. 139–144, 170.

[3]Hughes, W. F., and Young, F. J., *Electromagnetodynamics of Fluids*, Wiley, New York, 1966, p. 150.

[4]Capitelli, M. (ed.), *Nonequilibrium Vibrational Kinetics*, Springer–Verlag, Berlin, 1986.

[5]Butler, G. W., Kashiwa, B. A., and King, D. Q., "Numerical Modeling of Arcjet Performance," AIAA Paper 90-1474, June 1993.

[6]Miller, S. A., and Martinez-Sanchez, M., "Multifluid Nonequilibrium Simulation of Electrothermal Arcjets," AIAA Paper 93-2101, June 1993.

[7]Okamoto, H., Nishida, M., and Tanaka, K., "Numerical Studies of the Flow Field in a Low Power DC Arcjet Thruster Using Navier-Stokes Equations," 22nd International Electric Propulsion Conf., Viareggio, Italy, Oct. 1991 (Paper 91-112).

[8]Rhodes, R. P., and Keefer, D., "Numerical Modeling of an Arcjet Thruster," AIAA Paper 90-2614, July 1990.

[9]Megli, T. W., Krier, H., Burton, R. L., and Mertogul, A. E., "Two-Temperature Modeling of N_2/H_2 Arcjets," AIAA Paper 94-2413, July 1994.

[10]Babu, V., Aithal, S., and Subramaniam, V. V., "Vibrational Non-Equilibrium in Arcjet Flows," Paper 23rd International Electric Propulsion Conf., Seattle, WA, Sept. 1993 (Paper 93-129).

[11]Babu, V., and Subramaniam, V. V., "Numerical Solutions to Nozzle Flows with Vibrational Nonequilibrium," *Journal of Thermophysics and Heat Transfer*, Vol. 9, No. 2, 1995, pp. 227–232.

[12]Mitchner, M., and Kruger, C. H., *Partially Ionized Gases*, Wiley, New York, 1973, pp. 88–100, 146–155.

[13]Briley, W. R., and McDonald, H., "Solution of the Multidimensional Compressible Navier-Stokes Equations by a Generalized Implicit Method," *Journal of Computational Physics*, Vol. 24, No. 4, 1977, pp. 372–397.

[14]Anderson, D. A., Tannehill, J. C., and Pletcher, R. H., *Computational Fluid Mechanics and Heat Transfer*, Hemisphere, New York, 1984, p. 515.

[15]Isaacson, E., and Keller, H. B., *Analysis of Numerical Methods*, Wiley, New York, 1965, pp. 58–61.

[16]Glocker, B., and Auweter-Kurtz, M., "Radiation Cooled Medium Power Arcjet Experiments and Thermal Analysis," AIAA Paper 92-3834, July 1992.

[17]Gardiner, W. C., Jr., and Kistiakowsky, G. B., "Thermal Dissociation Rate of Hydrogen," *Journal of Chemical Physics*, Vol. 35, No. 5, 1961, pp. 1765–1769.

[18]Janev, R. K., Langer, W. D., Evans, K., Jr., and Post, D. E., Jr., *Elementary Processes in Hydrogen-Helium Plasmas*, Springer–Verlag, New York, 1987.